Available online at www.sciencedirect.com
ScienceDirect
Journal of Sound and Vibration 311 (2008) 1271–1285
JOURNAL OF SOUND AND VIBRATION
www.elsevier.com/locate/jsvi

Development of a directivity-controlled piezoelectric transducer for sound reproduction

Magella Bédard, Alain Berry*

Département de génie mécanique, Université de Sherbrooke, Sherbrooke, Canada J1K 2R1

Received 4 April 2006; received in revised form 24 September 2007; accepted 10 October 2007
Available online 26 November 2007

Abstract

Present sound reproduction systems do not attempt to simulate the spatial radiation of musical instruments, or sound sources in general, even though the spatial directivity has a strong impact on the psychoacoustic experience. A transducer consisting of 4 piezoelectric elemental sources made from curved PVDF films is used to generate a target directivity pattern in the horizontal plane, in the frequency range of 5−20 kHz. The vibratory and acoustical response of an elemental source is addressed, both theoretically and experimentally. Two approaches to synthesize the input signals to apply to each elemental source are developed in order to create a prescribed, frequency-dependent acoustic directivity. The circumferential Fourier decomposition of the target directivity provides a compromise between the magnitude and the phase reconstruction, whereas the minimization of a quadratic error criterion provides a best magnitude reconstruction. This transducer can improve sound reproduction by introducing the spatial radiation aspect of the original source at high frequency.

1. Introduction

A sound source such as a musical instrument is characterized by its intensity, its spectral and temporal attributes and its acoustic directivity in space [1]. In music or audio reproduction, it is desirable that the transducers reproduce the attributes of the original source as closely as possible. Actual sound system sources attempt to reproduce the intensity, the spectral and the temporal attributes of the original source, but generally cannot recreate directivity patterns, so it is usually not possible to reproduce the original source directivity. The reproduced directivity is therefore dependent on the directivity of the reproduction sources which in the case of conventional domestic loudspeaker systems are as omnidirectional as possible. However, the spatial directivity has a strong impact on the perception of presence and immersion [2]. Indeed, the spatial directivity of a musical instrument in a closed space is perceived by a fixed listener via relative contributions of the direct and reverberated sound emitted by the instrument; this mechanism creates a sense of spatial sound radiated by the source [3]. In a reproduction context using electroacoustic transducers, it would be interesting to project the sound with a directivity that approaches the directivity of the original source. The lack of

*Corresponding author. Tel.: +1 819 821 8000x2148; fax: +1 819 821 7163.
E-mail address: Alain.Berry@USherbrooke.ca (A. Berry).

0022-460X/$ - see front matter © 2007 Elsevier Ltd. All rights reserved.
doi:10.1016/j.jsv.2007.10.016

directivity reproduction in conventional electrodynamic drivers results in the impression that the sound does not emanate from the original source. A directivity-controlled transducer would overcome this limitation and produce a better psychoacoustic experience.

Some acoustic devices with useful fixed acoustic directivity were already developed and commercialized. Systems made of a plurality of electrodynamic drivers able to generate an omnidirectional radiation are available for room acoustics metrology (such as the Brüel and Kjaer type 4292 OmniPower sound source) or audio reproduction (such as the multi-facetted sources marketed by Solid Acoustics Co.). On the other hand, research efforts have long been devoted to the development of highly directive sound sources in the audible range. Acoustic devices based on the nonlinear interaction of directive ultrasound beams in air have been developed [4–6], resulting in ultra-directive audible sound radiation. Furthermore, loudspeaker linear arrays [7–9] or planar arrays [10] have been used to generate directional sound beams.

An approach for synthesizing a given radiation pattern from a collection of loudspeakers laid out on the facets of a cubic frame was recently developed [2]. Experimental results showed that the system can reproduce monopole, dipole and composites of these radiation patterns up to 2 kHz. Similarly, Weinreich filed a US Patent [3] to simulate directivity patterns of musical instruments with several sound sources in close proximity. Adjustable delays introduced between the sources result in constructive and destructive interferences, and controllable directivity patterns. However, this patent does not provide details on the method for directivity synthesis and the type and arrangement of transducers.

This paper describes a compact piezoelectric sound source with a controllable directivity. Poly(vinylidene fluoride) (PVDF) is a flexible piezoelectric material that provides the possibility to create shapes suitable for the design of a directivity-controlled transducer. Moreover, piezopolymers offer the possibility to develop loudspeakers with a very lightweight moving mass and therefore fast transient response. Since its discovery in the late 1960s by Kawai [11], PVDF was used for the design of several acoustic transducers. A good summary of piezoelectric loudspeakers using PVDF film can be found in Klapholz [12]. The first known audio application of this material was a ''planar'' loudspeaker designed in 1972 by Ohga [13,14]. In 1975, the first attempts to develop an omnidirectional piezoelectric tweeter, using two cylindrical PVDF transducers, were reported [15,16]. Others [17] later improved this principle by using several disc-shaped horns with hollow centers staked up around the pulsating cylinder. Subsequent work improved fabrication techniques to mould three-dimensional piezolectric polymer surfaces such as cones, portions of spheres, and corrugation [18]. In this work, the source is formed of several curved piezopolymer membranes arranged in a cylindrical shape and is specifically designed as a directivity-controlled transducer in the $5-20$ kHz range. In this study, control of directivity is aimed only in the horizontal plane (typically containing the listener's head) since sound localization is more easily achieved in the horizontal plane. The following sections present the principle used and the prototype, the vibration and acoustic response of an elemental (1/4 cylinder) source, and the acoustic directivity synthesis in the frequency and time domains. Finally, experimental results of acoustic directivity synthesis of a violin are shown to illustrate the spatial radiation capabilities of this transducer. It is shown that a very good reconstruction of the Sound Pressure Levels can be achieved in the horizontal plane, at the expense of a poor sound pressure phase reconstruction. Since phase is known to play a minor role in spatial localization by the auditory system in the frequency range investigated here, a poor phase reconstruction does not impair the subjective appreciation of the transducer.

2. Principle used and prototype

The principle used to design a directivity-controlled transducer is shown in Fig. 1. It consists of four elemental sources covering each a quarter cylinder. A cylindrical geometry allows coupling the extensional and radial displacements of the piezoelectric material, and permits to create sound radiation in all the horizontal plane. Each source is excited independently by voltages inputs $U_i(\omega)$ so it is possible to create destructive and constructive interferences between sources and thus create directivity pattern in the horizontal plane.

The prototype built from this principle is shown in Fig. 2. Each elemental source (a) was made from a curved 28 μm PVDF film with silver ink metalization—Measurement Specialties part # 1-1004346-0—with two sides fixed on a rigid frame (b), while the top and bottom sides are free (e). The interior of the PVDF film (a) was filled with melamine foam (c). The role of the melamine is to maintain the curved shape of the PVDF,

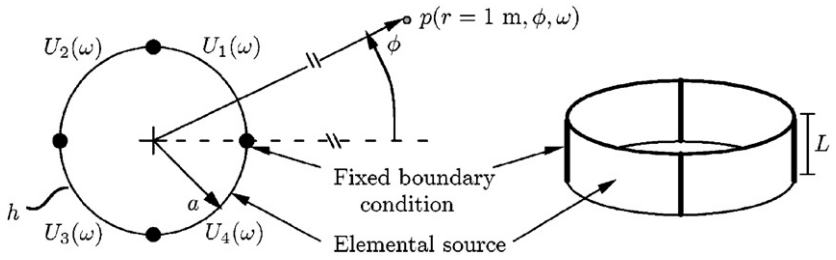

Fig. 1. Principle used and coordinate system. The $U_i(\omega)$ are the voltage inputs to individual sources.

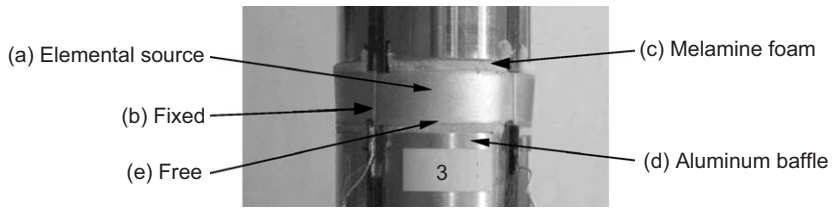

Fig. 2. Prototype.

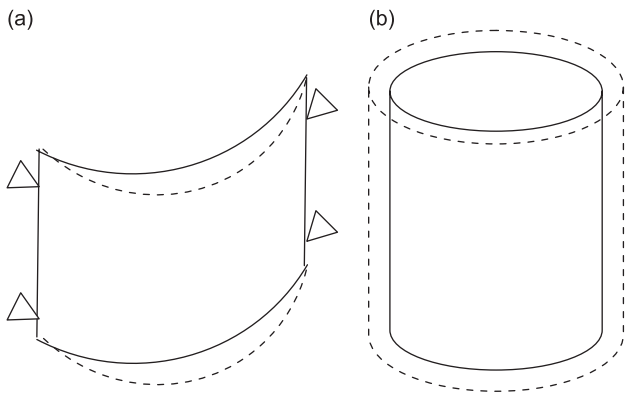

Fig. 3. Mode shapes: (a) $m = 0, n = 1$ flexural mode shape of a fixed-free cylinder and (b) breathing mode of a complete cylinder.

and provide sufficient sound absorption to prevent excitation of acoustic cavity modes. Finally, an aluminum baffle (d) was added on the free upper and lower sides of the transducer to prevent acoustic short circuit effects. The prototype's elemental sources have a radius of curvature a of 32 mm and a height L of 15 mm (see Fig. 1). A Young's modulus E of 4 GPa, a Poisson coefficient v of 0.18, a density ρ of 1780 kg/m^3 and piezoelectric strain constants $d_{31} = 22\,\mathrm{pC/N}$, $d_{32} = 3\,\mathrm{pC/N}$ and $d_{33} = -30\,\mathrm{pC/N}$ were used for the PVDF, as given by Measurement Specialities Inc. The damping ratio was approximated experimentally to be 0.25. These values will be used for all results shown in this paper, unless otherwise mentioned.

The strain of the PVDF membrane produced by an applied electric field generates a radial displacement of the film such that the piezoelectric effect predominantly excites the mode $m = 0$, $n = 1$, where m is the longitudinal mode order and n is the circumferential mode order for a fixed-free quarter cylinder (Fig. 3(a) shows the corresponding mode shape of the PVDF membrane). The radial motion of the film subsequently generates sound.

3. Vibration response of an elemental source

An elemental source is defined as a PVDF 1/4 cylinder shell driven by a uniform electric field in the radial direction. The boundary conditions are fixed on 2 opposite sides, the other 2 sides being free. As a preliminary

step, the modes of a purely elastic shell were calculated for a PVDF 1/4 cylindrical shell with simply supported boundary conditions following [19–22] and for a circular PVDF ring having the same radius as the elemental source. Of particular interest here, is the ring frequency of the PVDF cylindrical shell, which corresponds to the breathing mode ($n = 0$, n: circumferential mode order) and is given by

$$f_r = \frac{1}{2\pi a}\sqrt{\frac{E}{\rho(1-\nu^2)}}. \tag{1}$$

The breathing mode of a complete cylindrical shell is shown in Fig. 3(b). It was found that the natural frequency of the breathing mode closely matches the natural frequency of the $m = 0$, $n = 1$ mode of the fixed-free cylinder [22] (m and n are, respectively, longitudinal and circumferential mode orders). Consequently, the elemental source is expected to be an efficient radiator in the ring frequency region. The ring frequency of the prototype transducer is approximately $f_r = 7.6\,\text{kHz}$. The radius a was actually selected to have the ring frequency in the useful frequency range (5−20 kHz) of the transducer. In the case of the forced response of the elemental source under a uniform transverse electric field applied across the PVDF electrodes, only the odd–odd circumferential and longitudinal modes are excited.

A simple small displacement model proposed by Edelman and Dereggi [23] for a curved piezoelectric polymer sheet pinned at the edges suggests that the radial displacement is independent of the longitudinal position and depends on the circumferential position according to

$$w = \frac{a\gamma d_{31} U(t)(\sin\phi - \cos(\gamma/2))}{2h(\sin(\gamma/2)) - (\gamma/2)\cos(\gamma/2)}, \tag{2}$$

where ϕ and γ are defined in Fig. 4, h is the polymer thickness and $U(t)$ is the time-dependent voltage applied to the piezoelectric polymer. In the case of the elemental source, the above equation reduces to

$$w = \frac{5.18 a d_{31} U(t)(\sin\phi - \sqrt{2}/2)}{h}. \tag{3}$$

This equation assumes that the PVDF film is massless and its shape remains circular. A more detailed analysis of the vibration response of the elemental source was conducted using the Finite Element Method under Ansys Multiphysics 8.1. The *in-vacuo* finite element model is shown in Fig. 5(a). In this model, the elastic shell element *SHELL63* was used to represent the PVDF film. To simulate the piezoelectric behavior of the elastic shell elements, an analogy between the piezoelectric linear equations and thermal equations was used. With this approach, an harmonic analysis consists of imposing a fluctuating temperature equal to the electric field and thermal expansion coefficients equal to strain piezoelectric constants [24,25].

The fluid-loaded finite element model is shown in Fig. 5(b). The *FLUID30* element is a 3D acoustic element which was used for modeling the fluid medium and the interface between the fluid and the PVDF structure.

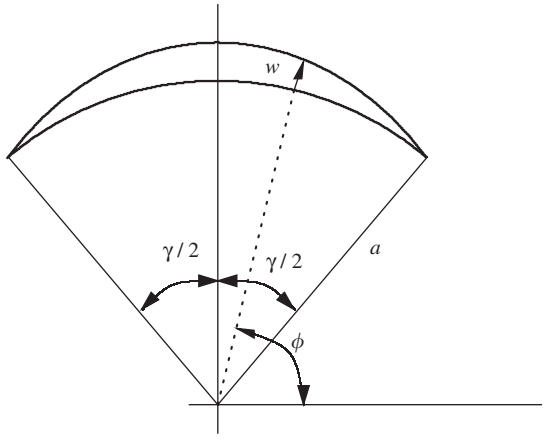

Fig. 4. Variables for Eq. (2).

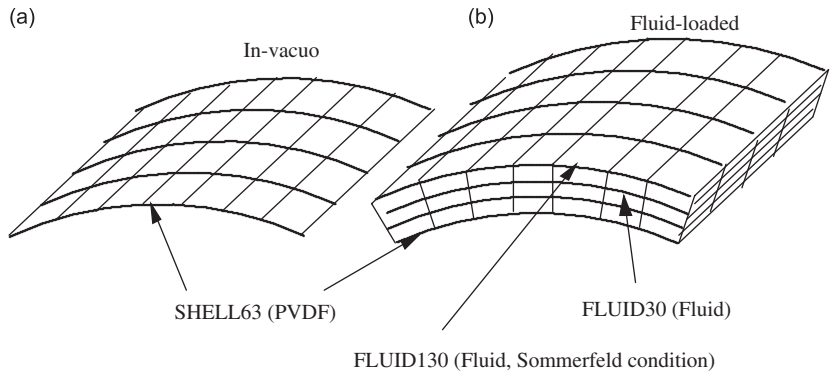

Fig. 5. Finite element model of a cylindrical circular shell under Ansys Multiphysics 8.1: (a) *In-vacuo* and (b) fluid-loaded.

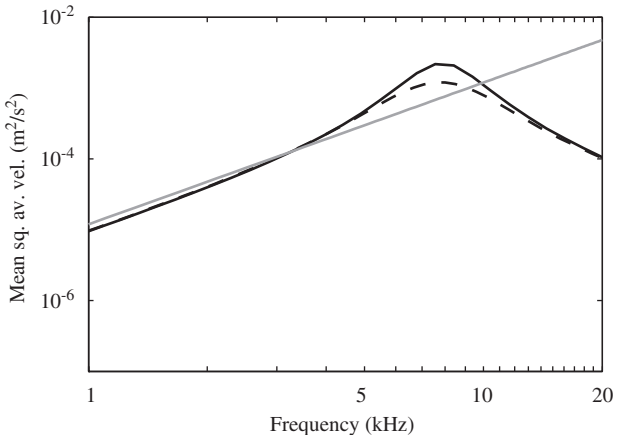

Fig. 6. Theoretical mean square averaged velocity calculated with the *in-vacuo* Finite Element model (black), fluid-loaded Finite Element model (black dashed) and Eq. (3) (gray), for a $20\,V_{rms}$ excitation.

The *FLUID130* element is a 3D infinite acoustic element that was used to account for outward wave propagation in the fluid domain that extends to infinity beyond the boundary of the finite *FLUID30* element.

Fig. 6 shows a comparison of results from the simple model (Eq. (3)) and finite element models *in-vacuo* and fluid-loaded, in terms of the spatially averaged mean square velocity of the elemental transducer, defined by $\langle \dot{w}^2 \rangle = \frac{1}{S}\int_S \frac{1}{2}|\dot{w}|^2\,dS$ where S designates the transducer area. These results correspond to an applied voltage of $20\,V_{rms}$ and a damping ratio value of 0.25 was assumed in the models. The peak of the vibration response corresponds to the ring frequency of the transducer. The simple model satisfactorily reproduces the 6 dB/oct increase of the transducer response below the ring frequency.

Air-loading decreases the vibration response in the ring frequency region because of the radiation damping effect. Moreover, the natural frequency is slightly decreased by the air loading of the transducer. Physically, this is associated with the additional fluid mass being set in motion by the transducer. Therefore, the surrounding air significantly affects the motion of the PVDF membrane in the vicinity of the ring frequency. In the rest of the paper, all structural and acoustical results are obtained with the fluid-loaded finite element model.

4. Acoustical response of an elemental source

4.1. Theory

A very simple compact source model can be derived by assuming that the transducer behaves as an omnidirectional point source with a volume velocity

$$Q_s = \int_S \dot{w}\,\mathrm{d}S, \tag{4}$$

were $\dot{w}$ denotes the time derivative of w. Using Eq. (3), and assuming a harmonic time variation of the input voltage $U(t) = U\mathrm{e}^{\mathrm{j}\omega t}$ we obtain

$$Q_s = -0.11613\frac{\mathrm{j}\pi\omega a^2 d_{31} UL}{h}\mathrm{e}^{\mathrm{j}\omega t}, \tag{5}$$

where L is the longitudinal dimension of the transducer. Therefore, the spherically symmetric sound pressure field radiated is given by

$$p(R,t) = \frac{\rho_0}{\pi R}\frac{\mathrm{d}Q_s}{\mathrm{d}t}\mathrm{e}^{-\mathrm{j}kR} = 0.11613\frac{\rho_0\omega^2 a^2 d_{31} UL}{rh}\mathrm{e}^{\mathrm{j}\omega t}\mathrm{e}^{-\mathrm{j}kr}. \tag{6}$$

Eq. (6) assumes that the transducer is massless, and the physical dimensions of the source are negligible in comparison to the acoustic wavelength (the actual source diameter equals an acoustic wavelength at approximately 5 kHz). It shows that for a given voltage, the SPL generated is inversely proportional to the PVDF film thickness. A thickness of 28 μm was chosen for the prototype because that was the smallest value available from the manufacturer.

The acoustic response considering the vibratory behavior of an elemental source was calculated in two steps:

(1) The radial displacement response was computed using the Finite Element Method on Ansys Multiphysics 8.1.
(2) The acoustic radiation was calculated using this displacement field as an input in the Kirchhoff–Helmholtz theorem.

The acoustic radiation of a baffled cylindrical circular shell immersed in a fluid with Sommerfeld conditions can be calculated from the Kirchhoff–Helmholtz theorem. The development can be found in Refs. [26,27]. The final relations are:

$$p(M) = -\int_S \rho_0\omega^2 w(P) G(M,P)\,\mathrm{d}P, \tag{7}$$

where $p(M)$ is the sound pressure at the field point $M(r,\phi,z)$, $w(P)$ is the radial displacement at point $P(a,\phi_0,z_0)$ on the shell surface, ω is the angular frequency, ρ_0 is the density of air ($\rho_0 = 1.2\,\mathrm{kg/m^3}$) and $G(M,P)$ is the acoustic Green's Function given by

$$G(M,P) = -\frac{1}{4\pi^2}\sum_{n=0}^{+\infty}\varepsilon_n\cos[n(\phi-\phi_0)]\int_{-\infty}^{+\infty} q_n(\beta)\mathrm{e}^{\mathrm{j}k_z(z-z_0)}\,\mathrm{d}k_z, \tag{8}$$

where

$$\beta = (k^2 - k_z^2)^{1/2}, \tag{9}$$

$$\varepsilon_n = \begin{cases} 1 & \text{if } n = 0, \\ 2 & \text{if } n \neq 0, \end{cases} \tag{10}$$

$$q_n(\beta) = \frac{H_n^{(1)}(\beta r)}{\beta a H_n^{(1)'}(\beta a)}. \tag{11}$$

In Eqs. (8)–(11), a cylindrical coordinate system is used (Fig. 7). Also, k designates the acoustic wavenumber ($k = \omega/c_0$ where c_0 is the sound speed), and $H_n^{(1)}$ is the Hankel function of the first kind. As explained previously, the radial displacement over the elemental source $w(P)$ was computed using finite element models of Fig. 5 under Ansys Multiphysics 8.1. It was assumed that $w(P) = 0$ for all points outside the radiation surface.

Unfortunately, the Green's function of Eq. (8) cannot be evaluated analytically. It is however possible to derive a simpler far field approximation of Eq. (8). Considering the fact that the acoustic pressure will be

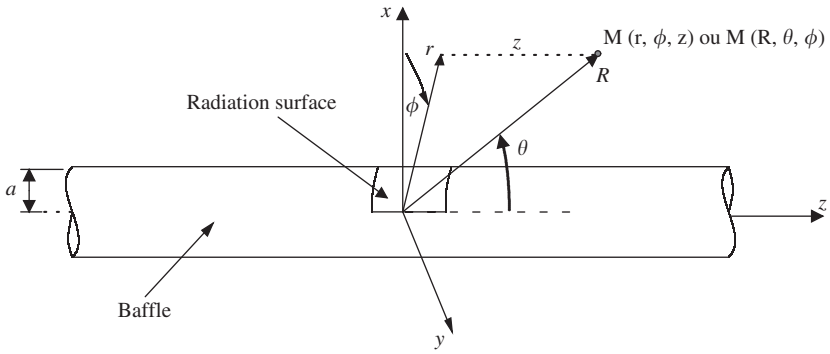

Fig. 7. Coordinates system.

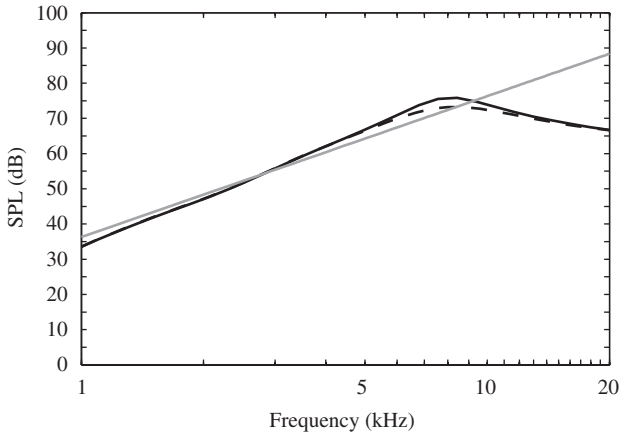

Fig. 8. Theoretical frontal sound pressure level calculated with the *in-vacuo* model (black), the fluid-loaded model (black dashed) and Eq. (6) (gray), for a $20\,V_{rms}$ excitation.

computed at 1 m from the source for a frequency range of 5−20 kHz (corresponding to between 15 and 60 wavelengths from the source), a far-field approximation is legitimate. The far-field acoustic pressure can be evaluated by the method of stationary phase [28]. It assumes that the contribution of regions where the modulus of the integrand varies slowly with k_z while the phase fluctuates quickly is negligible because regions with opposite phase and almost equal amplitude cancel each other. The resulting far-field expression is

$$G(M,P) = -\frac{1}{2\pi^2}\sum_{n=0}^{+\infty}\varepsilon_n \cos[n(\phi-\phi_0)]\frac{e^{-jn\pi/2}e^{-j\pi/2}e^{-jk\cos\theta z_0}e^{jkR}}{Rak\sin\theta H_n^{(1)'}(ka\sin\theta)}, \tag{12}$$

where (R,θ,ϕ) correspond to the spherical coordinates of M (see Fig. 7). In summary, the theoretical acoustic radiation of an elemental source is obtained at each frequency ω by a numerical evaluation of Eqs. (7) and (12).

The frontal sound pressure level which is calculated at $M(R = 1\,m, \theta = 90^\circ, \phi = 45^\circ)$, i.e. 1 m in front of an elemental source, is shown in Fig. 8. All results presented in this section are relative to the elemental source placed between $\phi = 0^\circ$ and 90°, to an excitation of $20\,V_{rms}$ and to a distance $R = 1\,m$. The results obtained from the *in-vacuo* and the air-loaded models (Eqs. (7) and (12)) and from Eq. (6) are presented. The sound pressure level is maximum at the ring frequency of the transducer and shows a 12 dB/oct slope before the ring frequency. This is due to the 6 dB/oct increase of the radiation efficiency of the breathing mode in low frequency combined with a 6 dB/oct increase of the transducer vibratory response below the ring frequency (Fig. 6). Furthermore, the maximum SPL appears in the 5−20 kHz band and is in the range of 65−73 dB for a $20\,V_{rms}$ excitation. Finally, we see that the simple monopole approximation of Eq. (6) provides a good approximation of the frontal sound radiation up to the ring frequency.

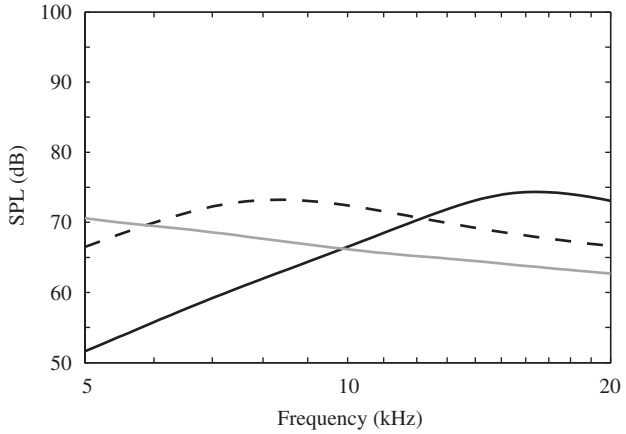

Fig. 9. Theoretical frontal sound pressure level at $R = 1$ m for $a = 16$ mm (black), $a = 32$ mm (black dashed) and $a = 64$ mm (gray), and for a 20 V_{rms} excitation.

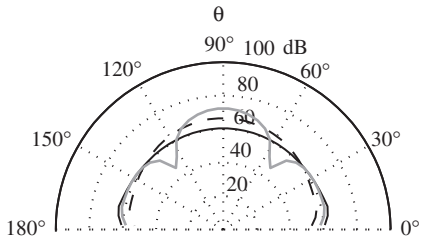

Fig. 10. Theoretical θ-directivity at $R = 1$ m and 20 kHz for $L = 7.5$ mm (black), $L = 15$ mm (black dashed) and $L = 30$ mm (gray), and for a 20 V_{rms} excitation.

Fig. 9 shows the frontal sound pressure level (at $M(R = 1\,\text{m}, \theta = 90^\circ, \phi = 45^\circ)$) generated by the elemental source for three values of the source radius. The maximum sound pressure level in each case does not change with the radius (and therefore the radiation area). However, the source radius affects the ring frequency (according to Eq. (1)) and therefore the useful frequency range of the source. In this case, a radius of 32 mm was chosen because it results in a fairly uniform acoustic response in the target frequency range of 5−20 kHz.

The axial dimension L of the prototype mainly influences the acoustic directivity in planes containing the source axis (θ-directivity, see Fig. 7).This is shown in Fig. 10 for a frequency of 20 kHz. For a large L, the elemental source is more directive than for a small L. In our case, the objective was to generate circumferential directivity patterns only (ϕ-directivity, see Fig. 7), while keeping the θ-directivity as omnidirectional as possible. A value of $L = 15$ mm allows to avoid θ-directivity lobes while slightly enhancing the front ($\theta = 90^\circ$) radiation of the source. This value was therefore selected for the prototype.

The influence of the frequency on the circumferential directivity for $\theta = 90^\circ$, and θ-directivity for $\phi = 45^\circ$, is shown in Fig. 11. The source is slightly more omnidirectional at low frequency. However, the frequency dependence of the acoustic directivity is not very pronounced in the 5−20 kHz range. Moreover, the difference between the front and the back radiation of the elemental source is approximately 15 dB over in this frequency range. As will be shown, these features make such a cylindrical source suitable for the control of directivity in the circumferential plane.

4.2. Experiments

Frequency response and directivity measurements of an elemental source were conducted in an anechoic room. A Brüel & Kjaer type 4189 prepolarized free-field 1/2″ Falcon^{TM} Microphone connected to a Brüel & Kjaer type 2671 DeltaTron® microphone preamplifier was placed at 1 m from the source axis. During the

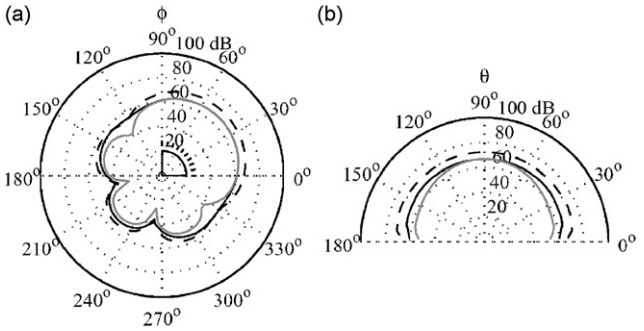

Fig. 11. Theoretical directivity at $R = 1$ m for 5 kHz (black solid), 10 kHz (black dashed) and 20 kHz (gray solid), and for a 20 V_{rms} excitation: (a) in the horizontal plane and (b) in the vertical plane.

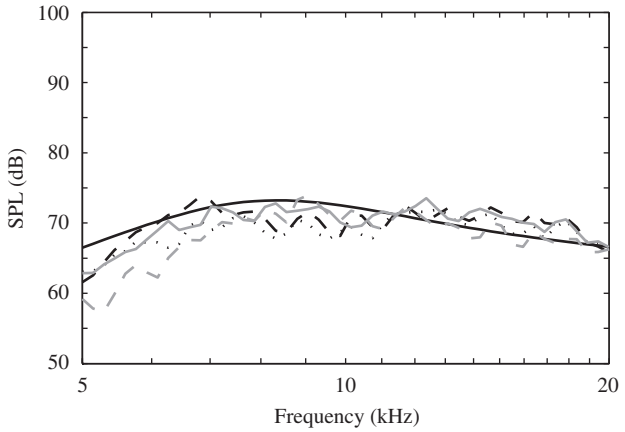

Fig. 12. Theoretical (black solid) and experimental frontal ($R = 1$ m, $\theta = 90°$) acoustic frequency responses for elemental source 1 (black dashed), 2 (black dotted), 3 (gray) and 4 (gray dashed), for a 20 V_{rms} excitation.

directivity measurements, the measuring microphone was fixed and the source was rotated (using a step motor) in small angular increments to obtain an almost continuous directivity plot. The PVDF membrane was driven via a PCB Piezotronics 790 series power amplifier with a sweeping sine in the 5−20 kHz range. A comparison between experimental and theoretical frontal sound pressure level (at $M(R = 1\,\text{m}, \theta = 90°)$) is shown in Fig. 12 for each of the four elemental sources. These measurements were conducted to investigate variations in acoustic responses of the 4 presumably identical radiators. Since directivity patterns are based on destructive/constructive interference of the 4 elemental radiators, it is important to initially verify that they have similar responses. During the measurements of these frequency responses, only one elemental source is active at the same time. The excitation voltage amplitude is 20 V_{rms}. Fig. 12 shows that, except for elemental source 4, the theoretical model estimates the experimental frequency response within a 5 dB deviation over the 5−20 kHz range. The oscillations in the experimental response are possibly caused by higher-order modes whose radiation efficiency may be larger than predicted by the model. Moreover the fairly large uncertainties on PVDF material properties used in the model, such as the Young's modulus, may explain deviations with the measurements. Finally, it should be noted that the silver-ink PVDF electrodes are not considered in the model, although their thickness (6 μm each) is not negligible compared to the PVDF thickness (28 μm). The sensitivity variations between elemental sources can be compensated in the directivity synthesis, as explained in Section 5.

In Fig. 13, experimental directivity results are compared to theoretical results for the elemental source 1 at 5, 10 and 20 kHz. The experimental data globally follow the predicted trends. However, circumferential directivity lobes are more marked in the theoretical data than in the experimental data, especially in low

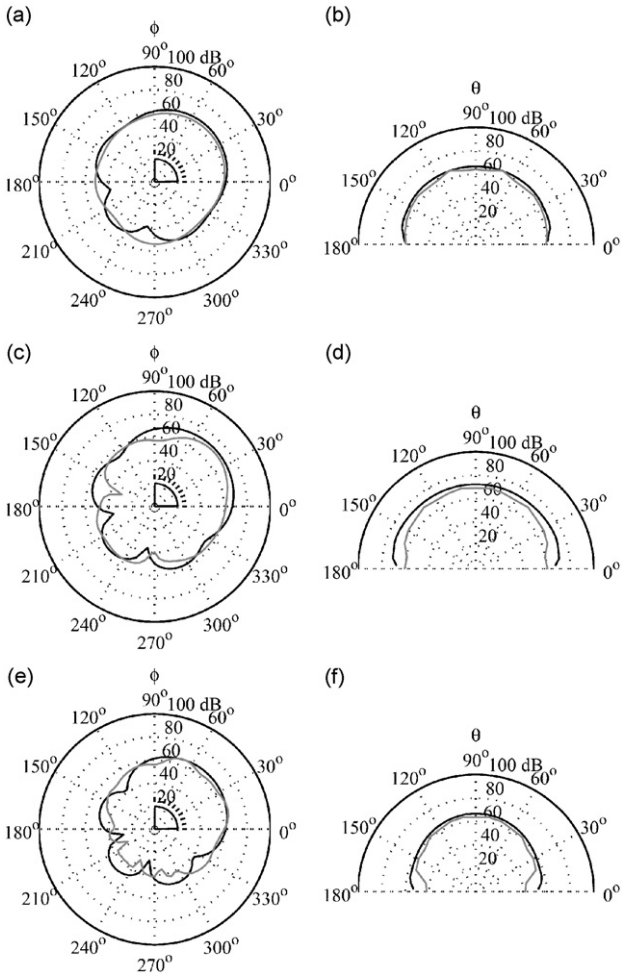

Fig. 13. Theoretical (black) and experimental (gray) directivity of elemental source 1 for an excitation of 20 V_{rms}: (a) in the horizontal plane at 5 kHz; (b) in the vertical plane at 5 kHz; (c) in the horizontal plane at 10 kHz; (d) in the vertical plane at 10 kHz; (e) in the horizontal plane at 20 kHz; (f) in the vertical plane at 20 kHz.

frequency. Moreover, at 20 kHz, the sound pressure level difference between the front and the back of the elemental source is slightly more pronounced in the experimental data than in the theoretical results. Nevertheless, similar to the theoretical results, the experimental directivity does not change a lot with frequency between 5 and 20 kHz.

5. Directivity synthesis in the frequency domain

In reference to Fig. 1, the problem of directivity synthesis is to derive appropriate input signals $U_i(\omega)$, $i = 1, \ldots, 4$ to the 4 elemental sources in order to create a target sound pressure far-field with a given circumferential directivity $p_t(\phi, \omega)$. For convenience, the target and reconstructed acoustic fields will be considered at $R = 1$ m from the source in the remainder of the text. Note that the target sound pressure field is *a priori* a complex valued function, therefore the source should reconstruct both the amplitude and phase distribution of the sound field in various circumferential directions. Fig. 14 shows the block diagram representation of the directivity synthesis problem in the frequency domain. The transducer inputs $U_i(\omega)$, $i = 1, \ldots, 4$ are obtained by filtering a single audio input $S(\omega)$ by appropriate filters $G_i(\omega)$, $i = 1, \ldots, 4$.

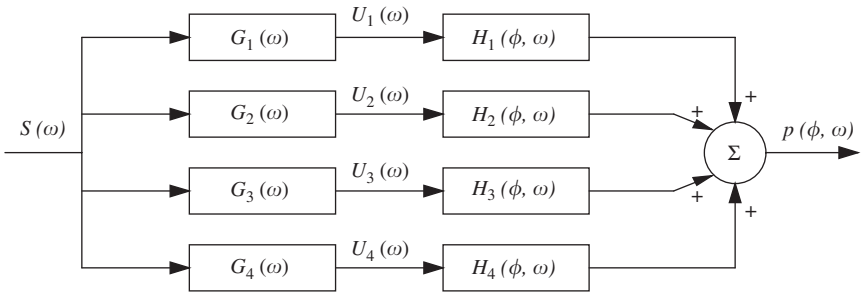

Fig. 14. Block diagram representation of the directivity synthesis in the frequency domain.

Introducing circumferential sound pressure field transfer functions of individual sources

$$H_i(\phi,\omega)=\frac{p_i(\phi,\omega)}{U_i(\omega)}, \tag{13}$$

where $p_i(\phi,\omega)$, $i=1,\ldots,4$ is the complex acoustic pressure produced by source i and $U_i(\omega)$ is the complex excitation voltage of source i. The total sound pressure $p(\phi,\omega)$ produced by the four sources is

$$p(\phi,\omega)=\mathbf{H}^{\mathrm{t}}(\phi,\omega)\mathbf{U}(\omega), \tag{14}$$

where $\mathbf{U}=\{U_1,U_2,U_3,U_4\}^{\mathrm{t}}$ and $\mathbf{H}=\{H_1,H_2,H_3,H_4\}^{\mathrm{t}}$. Since the transfer functions H_i are not orthogonal functions of the circumferential angle ϕ, it is more convenient to transform the decomposition (14) over orthogonal functions. This is accomplished by the following circumferential Fourier series of the target circumferential sound pressure field:

$$p_t(\phi,\omega)=a_0(\omega)+\sum_{n=1}^{\infty}(a_n(\omega)\cos n\phi+b_n(\omega)\sin n\phi), \tag{15}$$

where $a_0(\omega)$, $a_n(\omega)$ and $b_n(\omega)$ are the Fourier series coefficients, given by

$$a_0(\omega)=\frac{1}{2\pi}\int_0^{2\pi}p_t(\phi,\omega)\,\mathrm{d}\phi, \tag{16}$$

$$a_n(\omega)=\frac{1}{\pi}\int_0^{2\pi}p_t(\phi,\omega)\cos n\phi\,\mathrm{d}\phi, \tag{17}$$

$$b_n(\omega)=\frac{1}{\pi}\int_0^{2\pi}p_t(\phi,\omega)\sin n\phi\,\mathrm{d}\phi. \tag{18}$$

The coefficient a_0 represents the contribution of the monopole component of the target sound pressure field, while a_n and b_n represent orthogonal multipole components. Since the prototype source involves 4 independent radiators, only the monopole component a_0, 2 orthogonal dipole components a_1 and b_1, and a single quadrupole component b_2 can be synthesized in theory. Therefore, the Fourier series is truncated to 4 terms,

$$p_t(\phi,\omega)=\mathbf{A}^{\mathrm{t}}(\omega)\{1,\cos\phi,\sin\phi,\sin 2\phi\}^{\mathrm{t}}, \tag{19}$$

where $\mathbf{A}(\omega)=\{a_0(\omega),a_1(\omega),b_1(\omega),b_2(\omega)\}^{\mathrm{t}}$. Equating the target and reproduced sound fields, $p_t(\phi,\omega)=p(\phi,\omega)$, and using Eqs. (11), (16), (17), (18), we obtain

$$\mathbf{A}(\omega)=\mathbf{M}(\omega)\mathbf{U}(\omega), \tag{20}$$

where the coefficients of $\mathbf{M}(\omega)$ are given by

$$M_{1i}(\omega) = \frac{1}{2\pi}\int_0^{2\pi} H_i(\phi,\omega)\,\mathrm{d}\phi, \tag{21}$$

$$M_{2i}(\omega) = \frac{1}{\pi}\int_0^{2\pi} H_i(\phi,\omega)\cos\phi\,\mathrm{d}\phi, \tag{22}$$

$$M_{3i}(\omega) = \frac{1}{\pi}\int_0^{2\pi} H_i(\phi,\omega)\sin\phi\,\mathrm{d}\phi, \tag{23}$$

$$M_{4i}(\omega) = \frac{1}{\pi}\int_0^{2\pi} H_i(\phi,\omega)\sin 2\phi\,\mathrm{d}\phi. \tag{24}$$

The input signals of the elemental sources are thus given by

$$\mathbf{U}(\omega) = \mathbf{M}^{-1}(\omega)\mathbf{A}(\omega). \tag{25}$$

In brief, the approach involves calculating the Fourier coefficients a_0, a_1, b_1 and b_2 of the target sound pressure field, and identifying the circumferential sound pressure field transfer functions H_i of the elemental sources. This information is subsequently used in Eq. (25) to obtain the input signals $U_i(\omega)$ of the elemental sources to reproduce the target circumferential sound pressure field.

The previous approach allows both magnitude and phase reconstruction of the target sound field. However, from a perceptive view point, the human auditory mechanisms of sound localization in the high-frequency region of the audible spectrum are dominated by Interaural Envelope Time Shifts rather than Interaural Carrier Time Shifts [29]. Therefore, a magnitude reconstruction of the target sound field directivity would provide a sufficient psychoacoustic experience in the frequency range of interest. This can be simply accomplished via the minimization of the following criterion:

$$J(\omega) = \int_0^{2\pi}\left[\log_{10}\left(\frac{|p_t(\phi,\omega)|}{|p(\phi,\omega)|}\right)\right]^2\mathrm{d}\phi = \int_0^{2\pi}\left[\log_{10}\left(\frac{|p_t(\phi,\omega)|}{|\mathbf{H}^{\mathbf{t}}(\phi,\omega)\mathbf{U}(\omega)|}\right)\right]^2\mathrm{d}\phi. \tag{26}$$

The complex optimal inputs $\mathbf{U}(\omega)$ that minimize J are found using a multidimensional unconstrained nonlinear minimization technique implemented in the `fminsearch` Matlab function.

Prior to calculating the optimal source inputs $\mathbf{U}(\omega)$ using either Eq. (25) or the minimization of Eq. (26), it is appropriate to optimally orient the target sound directivity (or the transducer) in the circumferential direction. As a matter of fact, the four elemental sources can generate a dipole with an arbitrary circumferential orientation, but only a fixed quadrupole in space (the directions of null sound pressure corresponding to the

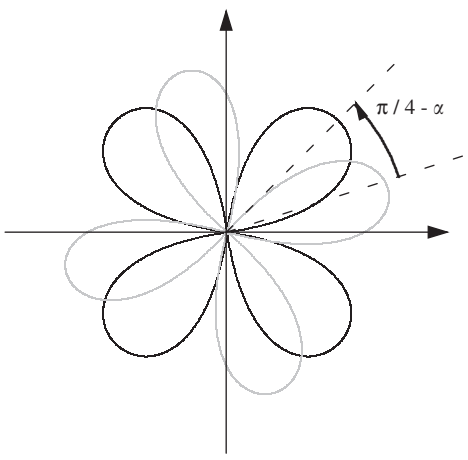

Fig. 15. Optimal orientation of the target acoustic pressure field corresponding to $\pi/4-\alpha$. The quadrupole that can be generated by the transducer is shown in black and the quadrupole contribution of the target acoustic field is shown in gray.

boundaries of the elemental radiators). It is therefore desirable to orient the quadrupole contribution of the target sound field in the same direction than the quadrupole that can be generated by the transducer (see Fig. 15). This optimal orientation is derived from the orientation of the quadrupole contribution $Q = a_2 \cos 2\phi + b_2 \sin 2\phi$ of the target sound field, where a_2 and b_2 are given by Eqs. (17) and (18). The directions α of the quadrupole's maxima and minima found from $\frac{d|Q|^2}{d\phi} = 0$ are

$$\alpha = \frac{1}{4}\tan^{-1} R + \frac{n\pi}{4}, \tag{27}$$

where n is an integer and

$$R = \frac{a_2 b_2^* + b_2 a_2^*}{|a_2|^2 - |b_2|^2}. \tag{28}$$

In Eq. (28), * designates the complex conjugate. In the interval $[0, \pi/2]$, there is one value of α that corresponds to a minimum of $|Q|^2$ and one value that corresponds to a maximum of $|Q|^2$. In order to properly orient the quadrupole contribution, a rotation equal to $\pi/4 - \alpha$ must be accomplished (see Fig. 14), where α corresponds to the value that maximizes $|Q|^2$ in $[0, \pi/2]$. The directivity synthesis therefore leads to considering the target sound field $p_t(\phi - \alpha + pi/4)$ instead of $p_t(\phi, \omega)$.

6. Elemental source inputs in the time domain

In the last section, two approaches were developed to derive the elemental source inputs $U_i(\omega)$, $i = 1, \ldots, 4$ in the frequency domain in order to synthesize the target sound pressure field. Referring to Fig. 14, the 4 elemental source inputs are obtained by passing the mono-channel audio input $S(\omega)$ through filters $G_i(\omega)$, $i = 1, \ldots, 4$. The frequency response of these filters is given by $G_i(\omega) = U_i(\omega)/S(\omega)$. The corresponding impulse responses are thus given by $g_i(t) = F^{-1}(U_i(\omega)/S(\omega))$ where F^{-1} denotes the inverse Fourier Transform.

In practice, the filter impulse responses were computed using causal Finite Impulse Response (FIR) digital filters: the time signals were sampled at the sampling frequency f_s, and the frequency responses $G_i(\omega) = U_i(\omega)/S(\omega)$ were thus sampled at frequencies $[0, \Delta f, 2\Delta f \ldots f_s/2]$ where $\Delta f = f_s/N$ and N is the number of samples. Note that zero-padding of the frequency responses was applied, meaning that the frequency responses $G_i(\omega)$ in the frequency range $[0, f_s/2]$ were taken to be zero at frequencies outside the operating frequency range $[5, 20]$ kHz of the transducer. An inverse Fast Fourier Transform was applied on $G_i(\omega)$ to obtain the sampled impulse responses $g_i(n)$. Since the inverse Fourier Transform of $G_i(\omega)$ generally results in non-causal impulse responses, the impulse responses were delayed by $N/2$ points, to yield $g_i(n - N/2)$. The input signals to the individual elemental sources $u_i(n)$ were then obtained by convolving the sampled audio input $s(n)$ with the delayed impulse responses $g_i(n - N/2)$.

7. Experimental results of acoustic directivity synthesis

In order to illustrate the approach, the acoustic radiation of the violin was used as the target acoustic pressure field $p_t(\phi, \omega)$. The spatial sound radiation of the violin was investigated by Otčenášek and Syrový [30]. In their work, the violin was excited artificially with the physical presence of the player, and the radiated sound was recorded at different frequencies with 16 microphones around the instrument. Since this work reports only non-dimensional acoustic directivity indexes, the phase was arbitrarily chosen to be constant in the circumferential direction and an average sound pressure level of 55 dB at 1 m was assumed.

The directivity synthesis processing was developed under National Instruments LabVIEW 7.1. The acquisition and the generation of the signals were done with a M-Audio Delta 44 sound card. A sampling frequency $f_s = 96$ kHz was chosen and the size of the sampled impulse responses was $N = 128$ points. The reconstructed circumferential sound pressure was measured using the setup detailed in Section 4.

The target directivity of the violin at 9 kHz is shown in Fig. 16, together with the definition of the orientation for the violin directivity. The experimental results obtained at 10 kHz using the circumferential Fourier decomposition of the target directivity (Eq. (25)) are shown in Fig. 16(a). The results obtained at

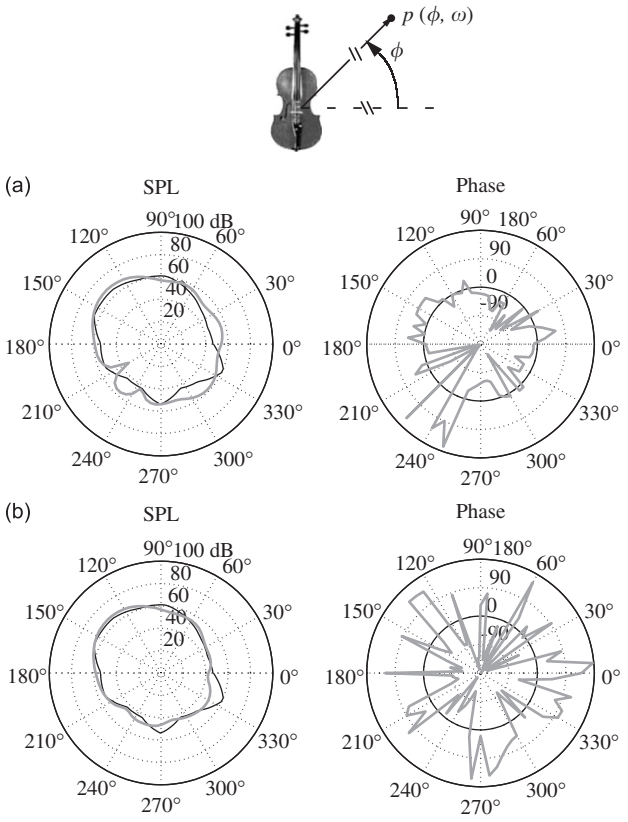

Fig. 16. Experimental reproduction of the 9 kHz violin directivity (black) at 10 kHz with (a) Fourier series and (b) the minimization of Eq. (26) (gray).

10 kHz using the minimization of criterion (26) are shown in Fig. 16(b). The results show that the target directivity is correctly reconstructed with only 4 sources. The Fourier decomposition approach provides a compromise between the magnitude and the phase reconstruction. On the other hand, the minimization approach provides the best magnitude reconstruction, at the expense of a poor phase reconstruction. Similar reconstruction results have been obtained for other frequencies between 5 and 20 kHz. Since interaural phase difference is known to play a minor role in spatial localization by the auditory system as compared to interaural intensity difference in the frequency range investigated here, a poor phase reconstruction does not impair the subjective appreciation of the transducer. Therefore, we believe that the approach using only magnitude reproduction of the sound field would provide a convincing spatial experience of the original source.

8. Conclusions

We have described a compact acoustic source consisting of four piezoelectric elemental sources made from curved PVDF films, that has the capability of projecting sound with a controllable circumferential directivity in the frequency range 5−20 kHz. The vibroacoustic analysis shows that sound is radiated by an elemental source through excitation and response of its fundamental membrane mode. The resonance of this fundamental mode can be approximated by the ring frequency of the transducer, which was 7.6 kHz in the case of the prototype presented. The sensitivity obtained was in the range of 65–73 dB at 1 m for a 20 V_{rms} excitation in the 5–20 kHz frequency range. Two approaches for circumferential directivity synthesis were proposed, allowing for reconstruction of both the magnitude and phase of the sound pressure field, or magnitude of the sound pressure field only. As an illustration of the directivity synthesis approach, the proposed transducer was used to emulate the acoustic directivity of a violin. The experimental results showed that the target directivity was correctly reconstructed with the 4 elemental sources.

Acknowledgments

This work was supported by Valorisation Recherche Québec (VRQ), and was conducted within Centre for Interdisciplinary Research in Music Media and Technology (CIRMMT), McGill University, Montreal.

References

[1] O. Warusfel, N. Misdariis, Directivity synthesis with 3d array of loudspeakers: application for stage performance, *Proceedings of the COST (the "European Co-operation in the field of scientific and Technical Research" program) G-6 Conference on Digital Audio Effects (DAFX-01)*, Limerick, Ireland, December 2001.
[2] O. Warusfel, N. Misdariis, T. Caulkins, E. Corteel, Radiation control applied to sound synthesis: an attempt for "spatial additive synthesis," *Journal of the Acoustical Society of America* 115 (5) (2004) 2528.
[3] G. Weinreich, Directional tone color loudspeaker, U.S. Patent No. 6,263,083, 2001.
[4] M.B. Bennett, D. Blackstock, Parametric array in air, *Journal of the Acoustical Society of America* 57 (1975) 562–568.
[5] M. Yoneyama, J. Ichiroh Fujimoto, Y. Kowamo, S. Sasabe, The audio spotlight: an application of nonlinear interaction of sound waves to a new type of loudspeaker design, *Journal of the Acoustical Society of America* 73 (5) (1983) 1532–1536.
[6] F.J. Pompei, The use of airborne ultrasonics for generating audible sound beams, *Journal of the Audio Engineering Society* 47 (9) (1999) 726–731.
[7] K.D. Jacob, T.K. Birkle, Prediction of the full-space directivity characteristics of loudspeaker arrays, *Journal of the Audio Engineering Society* 38 (4) (1990) 250–259.
[8] D.G. Meyer, Digital control of loudspeaker array directivity, *Journal of the Audio Engineering Society* 32 (10) (1984) 747–754.
[9] D. Klepper, D. Steele, Constant directional characteristics from a line source array, *Journal of the Audio Engineering Society* 11 (3) (1963) 198–202.
[10] M. Hawksford, Smart digital loudspeaker arrays, *Journal of the Audio Engineering Society* 51 (12) (2003) 1133–1162.
[11] H. Kawai, The piezoelectricity of poly(vinylidene fluoride), *Japan Journal of Applied Physics* 8 (7) (1969) 975–976.
[12] J. Klapholz, Polymer film for transducers, *DB, The Sound Engineering Magazine* 19 (6) (1985) 27–32.
[13] J. Ohga, Flat type loudspeaker using composite piezoelectric polymer material, *Meeting of the Institute of Electronics and Communication Engineers of Japan*, Japan, 1972.
[14] J. Ohga, A flat piezoelectric polymer film loudspeaker as a multi-resonance system, *Journal of the Acoustical Society of Japan* 4 (3) (1983) 113–120.
[15] M. Tamura, T. Yamaguchi, T. Oyaba, T. Yoshimi, Electroacoustic transducers with piezoelectric high polymer films, *Journal of the Audio Engineering Society* 23 (1) (1975) 21–26.
[16] K. Hatakeyama, S. Kinoshita, A. Haeno, T. Asanuma, Development of a loudspeaker system with omnidirectional high polymer tweeters, *The Proceedings of The Audio Engineering Society 52nd Convention*, New York, Ny, USA, 1975.
[17] B. Locanthi, K. Maekawa, K. Sugano, H. Fukura, S. Koyano, Development of a loudspeaker system with omni-directional horn loaded high polymer tweeter, *The Proceedings of The Audio Engineering Society 58th Convention*, New York, Ny, USA, 1977.
[18] F. Micheron, C. Lemonon, Moulded piezoelectric transducers using polar polymer, *Journal of the Acoustical Society of America* 64 (6) (1978) 1720–1721.
[19] W. Soedel, *Vibrations of Shells and Plates*, third ed., Marcel Dekker, New York, 2004.
[20] A.E.N. Love, On the small free vibrations and deformations of thin elastic shells, *Philosophical Transactions of the Royal Society of London* 179A (1888) 491–546.
[21] K. Forsberg, Influence of boundary conditions on the modal characteristics of thin cylindrical shells, *AIAA Journal* 2 (12) (1964) 2150–2157.
[22] M. Bédard, Development of a Controled Directivity Transducer for Sound Reproduction, Master's Thesis, Université de Sherbrooke, 2006 (in French).
[23] S. Edelman, A. Dereggi, Comments on "electroacoustic transducers with piezoelectric high polymer films," *Journal of the Audio Engineering Society* 24 (7) (1976) 577–578.
[24] F. Côté, Finite Element Development of the Active Region of a Multilayer, Intelligent Structure, Master's Thesis, Université de Sherbrooke, 2002 (in French).
[25] B. D. Freed, V. Babsusk, Finite element modeling of composite piezoelectric structures with MSC/NASTRAN, *SPIE fourth Annual Symposium on Smart Structures and Material: Smart Structures and Integrated Systems*, SPIE 3041, 1999, p. 676.
[26] C. Lesueur, Acoustic radiation of structures: vibroacoustics, fluid–structure interactions, *Collection de la Direction des Études et Recherches d'Électricité de France*, Eyrolles, Paris, 1988 (in French).
[27] E. G. Williams *Fourier Acoustics, Sound Radiation and Nearfield Acoustical Holography*, Academic Press, London, San Diego, 1999.
[28] M.C. Junger, D. Feit, *Sound, Structures, and their Interaction*, second ed., The MIT Press, London, 1986.
[29] J. Blauert, *Spatial Hearing, the Psychophysics of Human Sound Localization*, MIT Press, Cambridge, 1999.
[30] Z. Otčenášek, V. Syrový, Directivity of violin radiation, *The Journal of the Acoustical Society of America* 105 (2) (1999) 1330.